

Renewable Energy Research and Applications (RERA)



Vol. 6, No. 2, 2025, 251-258

DOI: 10.22044/rera,2025.14116.1420

Aeroacoustic Response of Turbine Blades to Rotational Speed and Angle of Attack Variations in Unsteady Flow Conditions

A. Khaleghi* and H. Bayat

1. Faculty of Mechanical Engineering Shahrood University of Technology, Shahrood, Iran.

Received Date 13 May 2025; Revised Date 27 June 2025; Accepted Date 27 June 2025 *Corresponding author: khaleghi79@yahoo.com (A. Khaleghi)

Abstract

The noise generated by a blade is assumed as one of the most central acoustic generation sources in a turbine. The sound induced by the movement of turbulent fluid over the turbine blade and its interaction with the surrounding environment causes the presence of vortices of different sizes in the turbulent flow. These vortices are considered as the major sources of acoustic waves in a wide range of frequencies. In the present study, the acoustic field induced by turbine blades is simulated by the aid of numerical simulation. In this respect, the flow field around the blades is solved by using the flow governing equations and then the acoustic solution of flow is modeled by using the Ffowcs Williams-Hawkings acoustic model. The main objectives of the present study include investigations of sound propagation at different distances of turbine axis, the extent of sound propagation along the blade direction, and the effect of the cavity implemented over the blade on acoustic results. The obtained results reveal that the sound pressure level generally decreases as the observer's distance increases. Furthermore, based on the obtained results, one can infer that the reduction in the sound pressure level is triggered by the presence of larger vortices with higher energy close to the blade (a larger sound pressure level) and smaller vortices at a further distance from the blade (a lower sound pressure level). Numerical simulations indicate that adding a cavity to the turbine blade does not reduce noise but instead increases the acoustic generation level.

Keywords: Turbine Aeroacoustics, Numerical Simulation, Sound Pressure level - SPL, Turbulent Flow Vortices, Ffowcs Williams-Hawkings Model - FW-H.

1. Introduction

The sound emitted from a turbine can be due to mechanical or aerodynamic factors. Mechanical noises stem from mechanical components such as the engine and gearbox, while aerodynamic sounds are caused by the blades that are chiefly interacting with the turbulent flow [1]. Lift force generation systems in flying objects are among the key contributors to acoustic generation [2]. At high angles of attack, these lift generation systems involve large vortices that if become combined and paired, then they yield a significant increase in the acoustic generation level.

Many numerical and experimental studies have been carried out to investigate the aero-acoustic phenomenon, namely the study conducted by Kuntz et al. [3]. Their results show that as the size of blades becomes smaller, the sound is decreased while the efficiency is reduced as a consequence. Hence, to compensate for this loss, they increased the rotational speed. Strawn and Biswas [4] investigated the acoustic signal of the helicopter

blade in a rotating and forward flight. In this regard, they applied the finite volume method to solve the Euler equation and used the Kirchhoff's integration to transmit the acoustic signal to the far-field flow. This study revealed that the acoustic fluctuations obtained at high speeds in the forward flight were in an acceptable with experimental agreement data. examination performed by Lieser et al. [5] on the aero-acoustics of a six-blade propeller indicated that the acoustic generation as dramatically reduced by decreasing the propeller size at a constant rotational speed. Fehse and Neise [6] studied the sound generated by a low-speed centrifugal fan. Jones et al. [7] designed an airfoil with lower acoustic generation by utilizing numerical simulation. Although this study excluded the 3D analysis of rotor performance, the results showed that airfoils with unusual shapes offered proper aerodynamic and aeroacoustic performances. Chapman [8] examined analytically aero-acoustic phenomenon at highspeed leading-edge noise. Kim et al. [9] studied the sound generated by the speed of the wind and its effects on the aerodynamic performance. The obtained results showed that the aerodynamic performance is enhanced by a reduction in the acoustic generation level. Coronado Domenge and Ilie [10] performed a numerical study on the helicopter blade using the flow theory where the effects of angle of attack, airfoil curvature, and size of vortices over the blade were addressed. Mohamed [11] studied the aerodynamic sound induced by the interaction of vortices at the trailing edge with the passing flow across the trailing edge, effects of speed, blade shape, and blade effects on the sound H-rotor Darrieus wind turbines. Moreover, in 2016, Mohamed investigated the sound generated by two different airfoils [12]. The conducted investigations were related to the distance between the two airfoils in each blade. The results demonstrated that once these two airfoils were mounted at a distance of 0.6C from each other, the best configuration was reached in terms of sound reduction. At last, Giauque et al. [13] studied and analyzed the aeroacoustic numerical simulation of the propeller. The study aims to evaluate the consequences of sound prediction and to reach an understanding of quadrupolar acoustic sources generated by flow like shock waves. The obtained results revealed that most quadrupolar sources are involved in the axial flow close to the propeller.

2. Governing equations

Consider incompressible Reynolds-averaged Navier-Stokes equations:

$$\frac{\partial u_j}{\partial x_j} = 0 \tag{1}$$

$$\rho \frac{\partial u_{i}}{\partial t} + \rho \frac{\partial u_{i} u_{j}}{\partial x_{j}} + \frac{\partial p}{\partial x_{j}} + \frac{\partial}{\partial x_{j}} \rho \left(\overline{u'_{i} u'_{j}} \right)$$

$$- \frac{\partial}{\partial x_{j}} \left(\mu \left(\frac{\partial u_{i}}{\partial x_{j}} + \frac{\partial u_{j}}{\partial x_{i}} \right) \right) = 0$$
(2)

where ρ , p, u are density, pressure, and velocity, respectively, and μ stands for the molecular viscosity of fluid. term $(\overline{u'_i u'_j})$ is called Reynolds stress tensor which is modeled, as follows:

$$\overline{u_i'u_j'} = \frac{2}{3}k\delta_{ij} - \mu_t(\frac{\partial u_i}{\partial x_i} + \frac{\partial u_j}{\partial x_i})$$
 (3)

k Rransport equation in the $k - \omega$ SST model is written in the tensor form as follows:

$$\rho \frac{\partial k}{\partial t} + \rho \frac{\partial}{\partial x_i} (u_i k) = \tag{4}$$

$$\frac{\partial}{\partial x_i} \left[\left(\mu + \frac{\mu_t}{\sigma_k} \right) \frac{\partial k}{\partial x_i} \right] + P_k - \beta^* \rho \omega k$$

where, μ_t is eddy viscosity and μ is molecular viscosity of the fluid. Also, P_k denotes the generation of turbulent kinetic energy caused by the interaction between the mean flow and turbulent flow field, given as follows:

$$P_{k} = \left[\mu_{t} \left(\frac{\partial u_{i}}{\partial x_{i}} + \frac{\partial u_{j}}{\partial x_{i}} \right) - \frac{2}{3} \rho k \delta_{ij} \right] \frac{\partial u_{i}}{\partial x_{j}}$$
 (5)

Term $\beta^* \rho \omega k$ in equation (4) presents the amount of turbulent kinetic energy dissipation. The transport equation for the second variable, i.e., ω , in the tensor form is as follows:

$$\begin{split} \frac{\partial \omega}{\partial t} + \rho \frac{\partial}{\partial x_i} (u_i \omega) &= \frac{\partial}{\partial x_i} \left[\left(\mu + \frac{\mu_t}{\sigma_\omega} \right) \frac{\partial \omega}{\partial x_i} \right] \\ + \frac{\rho \gamma}{\mu_t} \tau_{ij} \frac{\partial u_i}{\partial x_j} - \rho \beta \omega^2 + 2(1 - F_1) \sigma_{w2} \frac{1}{\omega} \frac{\partial k}{\partial x_j} \frac{\partial \omega}{\partial x_j} \end{split} \tag{6}$$

The available constant in these equations are calculated using the linear relation below:

$$\phi = \phi_1 F_1 + \phi_2 (1 - F_1) \tag{7}$$

where ϕ_1 and ϕ_1 stand for the following constants:

$$\sigma_{k1} = 0.85
\sigma_{\omega 1} = 0.5
\beta_1 = 0.075
\beta^* = 0.09
\gamma_1 = 5/4
\sigma_{k2} = 1.0
\sigma_{\omega 2} = 0.856
\beta_2 = 0.0828
\gamma_2 = 0.44$$
(8)

Replacing the blending functions $F_1 = 1$ and $F_1 = 0$ in the equations, the equations will be in the standard form of $k - \omega$ and $k - \varepsilon$, respectively. The blending function F_1 is defined below

$$F_{1} = tanh \left\{ \left\{ \min \left[\max \left(\frac{\sqrt{k}}{0.09\omega y}, \frac{500\mu}{y^{2}\omega\rho} \right), \frac{4\rho\sigma_{w2}k}{CD_{k\omega}y^{2}} \right] \right\}^{4} \right\}$$
 (9)

where y is the distance from the nearest wall and $CD_{k\omega}$ is expressed as follows:

$$CD_{k\omega} = \text{MAX}(2\rho\sigma_{w2}\frac{1}{\omega}\frac{\partial k}{\partial x_j}\frac{\partial \omega}{\partial x_j}, 10^{-20})$$
 (10)

After solving the transport equations, the eddy viscosity will be obtained by the following relation:

$$\mu_t = \frac{0.31 \,\rho k}{\text{MAX}(0.31\omega, \Omega F_2)} \tag{11}$$

where Ω is vorticity magnitude, which is defined below:

$$\Omega = \sqrt{\left(\frac{\partial u}{\partial y} - \frac{\partial v}{\partial x}\right)^2} \tag{12}$$

Moreover, F_2 will be obtained as follows:

$$F_2 = \text{TANH}\left(\left(\max\left(\frac{2\sqrt{k}}{0.09\omega y}, \frac{500\mu}{y^2\omega\rho}\right)\right)^2\right)$$
 (13)

To predict the far-field sound, the Ffowcs Williams-Hawkings acoustic model has been considered which is based on Lighthill acoustic analogy. In this method, some equations are required to predict sound, including RANS, DES, or LES equations. This acoustic differentiates the noise propagation process with sound generation and also the flow solution process from the acoustic analysis. This method is also used in the simulation software FLUENT and is based on the Ffowcs Williams-Hawkings method and its integral solution. This method is capable of predicting generated sound, including monopolar, bipolar, and quadrupolar sounds. Moreover, it employs time-dependent integral equations and calculates all acoustic signals in one period where the observers are located. The exact solution time of flow variables, namely pressure, velocity, and density in the sound source, is applied for the integral solution of the next step. In other words, variations of unsteady flow have been obtained by numerical computations and used as the input in the Williams-Hawkings equations to estimate the blade sound intensity. The exact solution time is reached by implementing turbulent flow solution models for the unsteady state.

The sound source in the Ffowcs Williams-Hawkings model can be applied not only for impermeable walls but also for permeable walls. Furthermore, this method is capable of defining multiple sound receivers to assess the strength of the propagated sound in different places in the vicinity of sound source. Assuming that the sound source is defined in an enclosure surface, the Ffowcs Williams-Hawkings differential equations will be as follows:

$$\frac{1}{C_0^2} \frac{\partial^2 P}{\partial t^2} - \nabla^2 p' = \frac{\partial^2}{\partial x_i \partial x_j} \Big(T_{ij} H(f) \Big)
- \frac{\partial}{\partial x_j} (p_{ij} n_j + \rho u_i (u_n - v_n)) \delta(f)$$

$$+ \frac{\partial}{\partial t} (\Big(\rho_0 v_n + \rho (u_n - v_n) \Big) \delta(f))$$
(14)

where is p' the far-field sound pressure ($p' = p - p_0$) and u_i is the velocity component in i direction. Moreover, u_n and v_n are the surface velocity components perpendicular to the plane. Generally, in this equation, the index i represents the component of each variable in x_i direction and the index n stands for the component perpendicular to the noise generation plane. $\delta(f)$ is the Dirac Delta function and H(f) is the Step function. Zero value of variable f includes noise generation surface (here turbine blade) and its larger values involve wave propagation zone. Moreover, the variables defined in the free flow are designated by 0 index. In equation (14), T_{ij} is Lighthill stress tensor which is defined as:

$$T_{ij} = \rho u_i u_j + p_{ij} - C_0^2 (\rho - \rho_0) \delta_{ij}$$
 (15)

 p_{ij} is the compressive stress tensor, which is defined for s tokes fluid as given below:

$$p_{ij} = p\delta_{ij} - \mu \left[\frac{\partial u_i}{\partial x_i} + \frac{\partial u_j}{\partial x_i} - \frac{2}{3} \frac{\partial u_k}{\partial x_k} \delta_{ij} \right]$$
 (16)

Here, the employed equation is a wave equation. There are three terms on the right side of this equation showing three heterogeneous acoustic sources. These sources consist of monopolar, bipolar, and quadrupolar sources. Monopolar, bipolar, and quadrupolar sources present the generated sound by the fluctuation of fluid mass due to the motion of planes, the fluctuations of force on the object surface, the fluctuations of fluid stresses, respectively. The Ffowcs Williams-Hawkings equation is solved with the aid of freespace Green's function $(\delta(g)/4\pi r)$. The complete solution is comprised of surface and volume integrals. The surface integral shows the portion of monopolar and bipolar sound sources as well as a fraction of quadrupolar sources while the volume integral displays the portion quadrupolar sound sources in the zones out of source planes. Once the flow is subsonic, the contribution of volume integral is reduced and therefore in FLUENT software it is considered.

$$p'(\vec{x},t) = P'_t(\vec{x},t) + P'_l(\vec{x},t) \tag{17}$$

$$4\pi p_l'(\vec{x},t) = \int_{f=0}^{\infty} \left[\frac{\dot{L_r}}{r(1-M_r)^2} \right] ds + \int_{f=0}^{\infty} \left[\frac{\rho_0 U_n (r\dot{M_r} + a_0 (M_r - M^2))}{r^2 (1-M_r)^3} \right] ds$$
(18)

$$4\pi p_l'(\vec{x}, t) = \frac{1}{a_0} \int_{f=0}^{\infty} \left[\frac{\dot{L_r}}{r(1 - M_r)^2} \right] ds + \int_{f=0}^{\infty} \left[\frac{\dot{L_r}}{r(1 - M_r)^2} \right] ds +$$
(19)

$$\frac{1}{a_0} \int_{f=0}^{\infty} \left[\frac{L_r(r\dot{M}_r + a_0(M_r - M^2))}{r^2(1 - M_r)^3} \right] ds$$

Also:

$$U_i = v_i + \frac{\rho}{\rho_0} (u_i - v_i)$$
 (20)

$$L_i = P_{ij}\hat{n}_i + \rho u_i(u_n - v_n) \tag{21}$$

Moreover, the retarded time τ is defined as follows:

$$\tau = t - \frac{r}{a_0} \tag{22}$$

where t is the given time of the observer and r is the distance from the observer.

3. Numerical results

This section addresses how boundary conditions are applied and the computational domain is meshed, followed by an investigation into the validation and independency of numerical solution from the mesh. In follows, the propagation of turbine-induced sound is examined at various distances from the blade. Furthermore, there is a comparison made between acoustic diagrams on receivers' sites at different distances from the turbine axis. The results obtained by the acoustic numerical simulation are presented for NACA0021. In addition, the sound pressure levelfrequency diagrams are provided for definite receivers and they are also comprehensively analyzed.

3.1. Numerical simulation method

In the present study, to separate rotating parts from non-rotating parts, the Multiple Reference Frame (MRF) is used. To simulate the blade by the sliding mesh method, rotation and non-rotating parts were meshed separately. The unsteady flow around the turbine blade is simulated two-dimensionally by employing ANSYS software. To discretize and solve the

fluid flow governing equations and couple the velocity and pressure equations, the PISO algorithm is implemented. To solve the turbulent problem, the two-equation model $k-\omega SST$ is applied. Furthermore, for the sake of a more accurate numerical solution, the fourth-order forward approximation and the fourth-order central difference approximation are used for the time derivative and local derivative, respectively. The computational domain is depicted in figure 1.

3.2. Numerical simulation method

The non-slip condition is used over the solid object (turbine blade) in the viscid flow and the pressure gradient is assumed to be zero on these surfaces. Uniform velocity is assumed for the inlet. Gradients of all variable (aside from pressure) are set zero at the outlet where the atmospheric pressure is incorporated. For the top and bottom boundary planes, the boundary condition of symmetry is applied in which the vertical gradient of velocity and, consequently, the shear stress on the boundary are perceived to be zero.

The computational domain is divided into rotating and non-rotating zones. The blades in the rotating zone are mounted with an angle of 120° from one another. To mesh the non-rotating and rotating zones, the structured and unstructured grids are used, respectively (Figures. 1-a and 1-b). Moreover, the boundary layer mesh is employed around the airfoil surface (Figures. 1-c and 1-d). To generate the mesh, Gambit software is utilized.

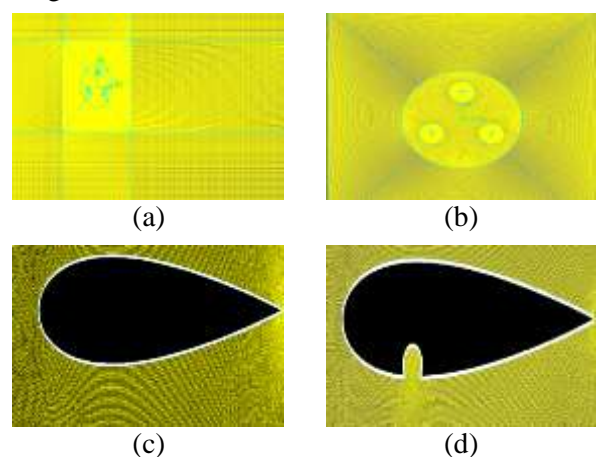


Figure 1. Computational domain, a) A full view of the computational domain, b) A close view of the rotating zone, c) The airfoil without cavity along with the boundary layer mesh, d) The airfoil with cavity along with the boundary layer mesh.

3.3. Numerical solution independency from computational domain mesh

To determine the sensitivity and independency to/from the computational mesh to solve the

problem, four different computational meshes are considered and their results are compared to one another. The specifications of the selected meshes are given in table 1. To evaluate the effect of mesh enhancement on the solution results, the number of cells around the airfoil is raised by a constant factor of 2. As can be observed in the table, variation percentage of turbine lift coefficient decreases by augmenting the number of cells around the airfoil. Furthermore, the values of lift coefficient are approximately the same for meshes No. 3 and 4.

Table 1. Investigation into the grid independency and the specification of meshes used in the simulation of airfoil NACA0012 at the angle of attack of 5.4° [14].

Grid	Number of cells	Numerical lift coefficient	Experimental lift coefficient [14]	Error
Grid 1	400532	0.35	0.56	37%
Grid 2	418156	0.42	0.56	25%
Grid 3	456357	0.530	0.56	5.5%
Grid 4	505765	0.538	0.56	4%

3.4. Validation of numerical solution

To validate the simulation, the obtained pressure coefficient is compared with the experimental data [15]. Figures. 2 through 4 compare the mean pressure coefficient data obtained from the $k-\omega$ sst method with the experimental data provided by Gregory and O'reilly [15]. As can be seen in these figures, the obtained numerical results satisfactorily agree with the experimental data.

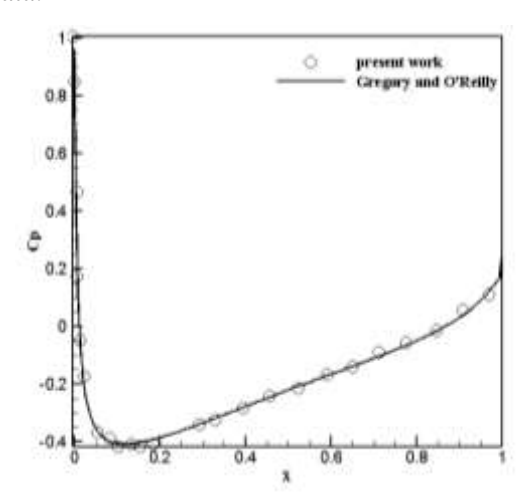


Figure 2. Comparison of pressure coefficient at the Reynolds number of $Re = 2.88 \times 10^6$ and AOA = 0 [15].

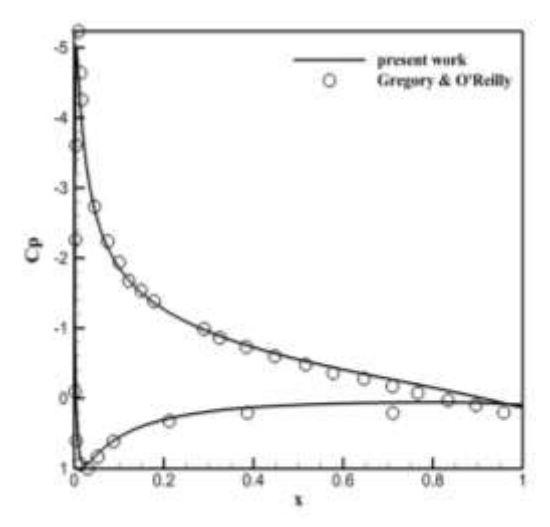


Figure 3. Comparison of pressure coefficient at the Reynolds number of Re = 2.88×10^6 and AOA = 10.8 [15].

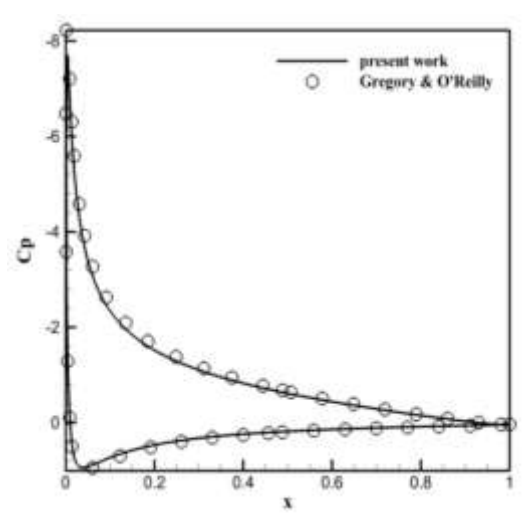


Figure 4. Comparison of pressure coefficient at the Reynolds number of $Re = 2.88 \times 10^6$ and AOA = 14.4 [15].

3.5. Validation of acoustic results

In this section, the accuracy of the predicted acoustic results are examined. The acoustic receiver in the laboratory, i.e., microphone, is located at the distance of 1.2 meter away from the trailing edge. The acoustic pressure is recorded at t = 1.5. The octave spectrum of data is compared with the experimental data presented by Wasala et al. [16], shown in figures 3 and 4. All numerical spectrums concur well with the experimental data. At AOA = 0, the maximum band frequencies have values below 2000 Hz. At larger angles of attack, the maximum band frequency does not occur. However, as the angle of attack is escalated, the rise in the sound pressure level (SPL) in the frequencies is lower than 2 kHz. As can be observed in these figures, the airfoil generates a high-frequency sound which is not largely dependent on angle of attack.

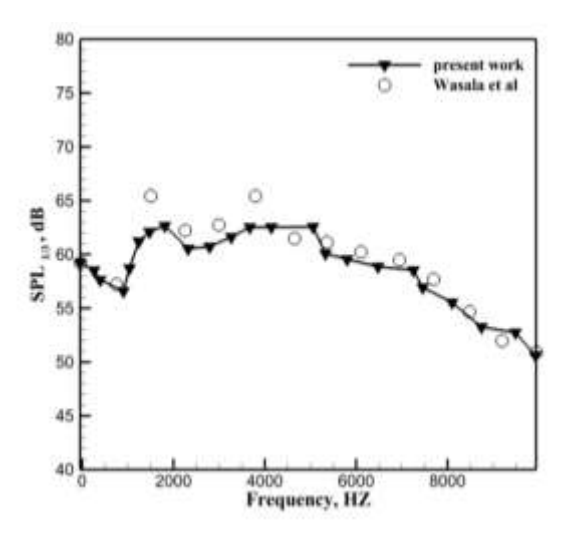


Figure 5. Diagram of acoustic validation at $Re = 2.88 \times 10^6$ and AOA = 0 [16].

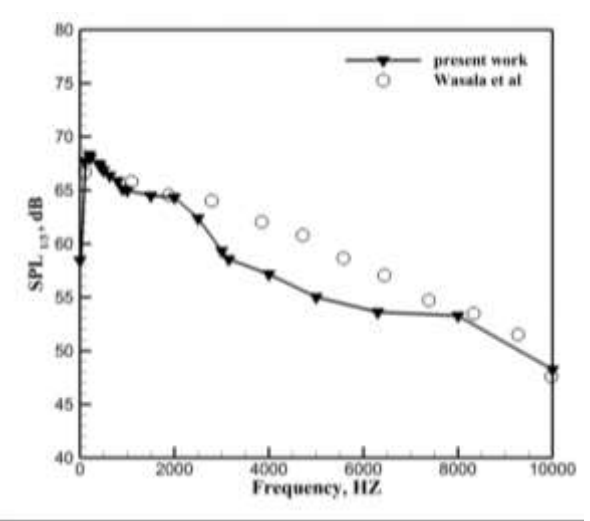


Figure 6. Diagram of acoustic validation at Re = 2.88×10^6 and AOA = 10 [16].

3.6. Evaluation of applying a cavity on turbine blade and its effects on acoustic results

To investigate the propagated noise at different distances from a turbine blade, sound receivers are located at constant distances from the turbine, i.e., constant radial distances of R=20C, 40C, 60C, and 80C. Figure 7 depicts the generated sound pressure level in terms of frequency on the receivers' site at constant radial distances of R=20C, 40C, 60C, and 80C without the presence of a cavity. It is evident that the maximum noise generation occurs in the vicinity of the turbine axis which can be attributed to the high sound generated by large vortices. These vortices are created due to the substantial turbulence of the flow close to the blades. However, at further distances from the axis, smaller vortices are the main origin of sound generation, implying a reduction in the propagated noise from the turbine by an increase in the distance from the sound source. This is attributed to the dissipation of acoustic wave energy along the traveled path and its conversion to heat.

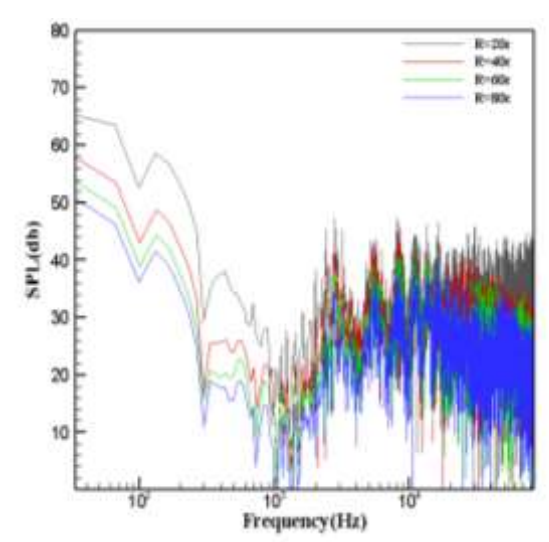


Figure 7. Comparison of the calculated sound pressure levels at constant radial distances of R=20C, 40C, 60C, and 80C without cavity.

To examine the effect of cavity formation on the obtained results of turbulent and acoustic fields, the simulation is carried out by creating a cavity at the distance of 0.25C in NACA0021 airfoil while assuming other geometric parameters to remain constant. The inlet fluid velocity and rotational speed of airfoil are set at 9 m/s and 42 rad/s, respectively. Figures 8 and 9 show the kinetic energy contour and diagrams of acoustic generation level for NACA0021 airfoil containing cavity at the pressure side, respectively. As can be observed in figure 9, the maximum sound pressure level is induced at frequencies lower than 100 Hz. Furthermore, by comparing the acoustic diagram at different distances from the axis, it can be concluded that the maximum propagated noise occurred at R=20C from the trailing edge across the airfoil axis direction. Generally, sound pressure level reached its maximum at the trailing edge of NACA0021 airfoil. After this point, the noise level was gradually reduced by getting away from the leading edge due to the dissipation of acoustic energy.

As aforementioned, the acoustic simulation for the airfoil NACA0021 is conducted by applying the turbulence model $k-\omega SST$ and the Ffowcs Williams-Hawkings acoustic model where the standard environmental conditions are considered for the surrounding. As can be seen in figure 10, comparing the acoustic diagrams at different rotational speeds of the airfoil, it can be concluded that the SPL generation increases by a rise in the rotational speed.

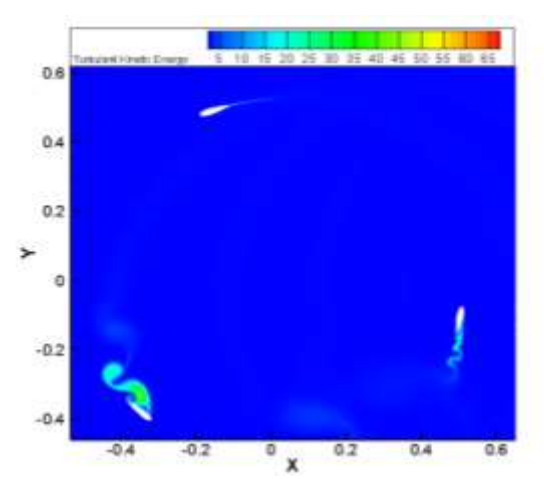


Figure 8. Contour of turbulent kinetic energy for NACA0021 airfoil.

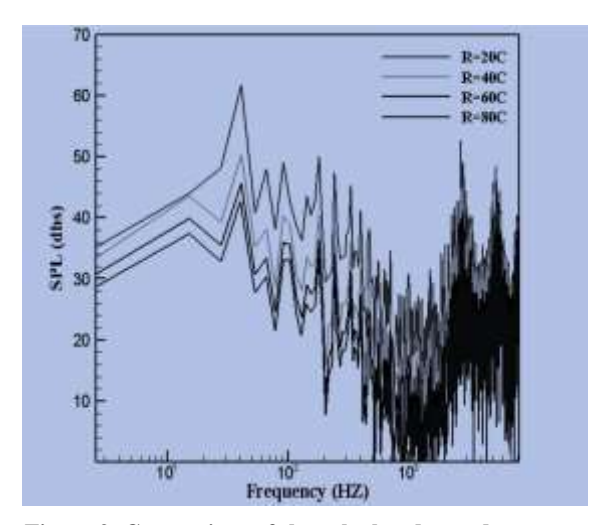


Figure 9. Comparison of the calculated sound pressure levels at constant radial distances of R=20C, 40C, 60C, and 80C containing cavity at the pressure side at the distance of 0.25 $\,\mathrm{C}$

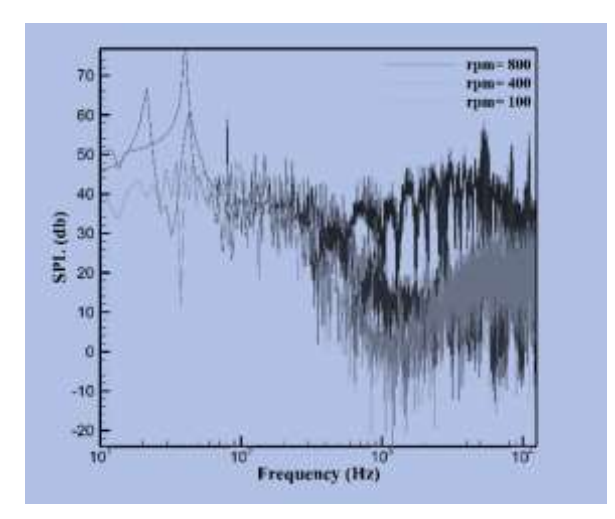


Figure 10. Comparison of the calculated sound pressure levels at different RPMs.

An increase in the angle of attack causes a change in the flow stream on the airfoil which can lead to augmenting the mixing and enlarging the generation of turbulent vortices that are the key cause of noise generation. According to figure 11, by increasing the angle of attack, the sound pressure level augments, provided that increasing the angle of attack does not lead to separation. Moreover, the sound pressure levels are provided in terms of frequency at constant radial distance of R=20C for three different locations, i.e., applying cavity at 0.25C, 0.5C, 0.75C on the airfoil pressure side. According to figure 12, pressure oscillations are higher by creating cavity on the airfoil, implying that the presence of a cavity lead to vortex formation and increase sound pressure levels.

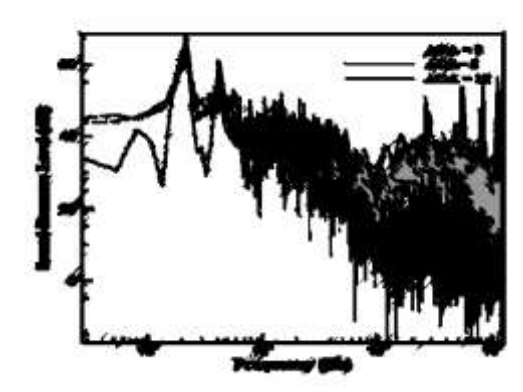


Figure 11. Comparison of the calculated sound pressure levels at different angles of attack.

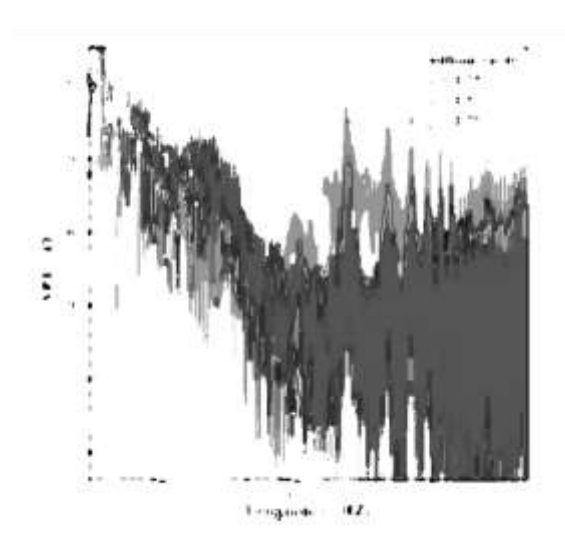


Figure 12. Comparison of the calculated sound pressure levels at constant radial distance of $R=20\mathrm{C}$ containing cavity at the pressure side at the distances of 0.25 C, 0.5 C, and 0.75 C

4. Conclusion

In the present study, the effects of rotational speed and angle of attack of an airfoil on the pressure fluctuations are investigated. The sound pressure level vs. frequency diagrams with\without cavity are considered for different states (i.e., at different RPMs of 100, 400, 800, at different angles of attack of 0°,5°,10°, and at constant radial distances of R=20C, 40C, 60C, 80C). The turbulent flow is used in which the sound and pressure fluctuations are mostly induced by vortices. The comparison of SPL diagrams for receivers revealed that pressure fluctuations increase at high rotational speed by raising the angle of attack of the airfoil NACA0021 to a certain value, while angles of attack larger than that cause a reduction in the SPL. This suggests that the rotational speed and increase in the angle of attack lead to the creation of vortices and sound increase, provided that they don't yield separation. Furthermore, sound pressure levels and pressure oscillations are higher by applying cavity on the airfoil, implying that the presence of cavity lead to vortex formation and increase sound level from an acoustic standpoint.

5. References

- [1] M. Ghasemian and A. Nejat, "Aero-acoustics prediction of a vertical axis wind turbine using Large Eddy Simulation and acoustic analogy," Energy, 88, pp. 711-717, 2015.
- [2] M. S. Mathias, E. M. Gennaro, and M. A. Medeiros, "Vortex generation and aeroacoustics in asymmetric wakes," Procedia IUTAM, 14, pp. 590-594, Jan 1, 2015.
- [3] M. Kuntz, D. Lohmann, and J. Lieser, "Comparison of rotor noise predictions by a lifting surface method and Euler solutions using Kirchhoff equation," in First CEAS/AQIAA Joint Aeroacoustic Conf, Munich, Germany, pp. 949-961, 1995.
- [4] R. C. Strawn and R. Biswas, "Numerical simulations of helicopter aerodynamics and acoustics," Journal of computational and applied mathematics, 66(1-2), pp. 471-483, 1996.
- [5] J. Lieser, D. Lohmann, and C. H. Rohardt, "Aeroacoustic design of a 6-bladed propeller," Aerospace science and technology, 1(6), pp. 381-389, 1997.

- [6] K.-R. Fehse and W. Neise, "Generation mechanisms of low-frequency centrifugal fan noise," AIAA journal, 37(10), pp. 1173-1179, 1999.
- [7] B. R. Jones, W. A. Crossley, and A. S. Lyrintzis, "Aerodynamic and aeroacoustic optimization of rotorcraft airfoils via a parallel genetic algorithm," Journal of Aircraft, 37(6), pp. 1088-1096, 2000.
- [8] C. J. Chapman, "Some benchmark problems for computational aeroacoustics," Journal of sound and vibration, 270(3), pp. 495-508, 2004.
- [9] T. Kim, S. Lee, H. Kim, and S. Lee, "Design of low noise airfoil with high aerodynamic performance for use on small wind turbines," Science in China Series E: Technological Sciences, 53(1), pp. 75-79, 2010.
- [10] P. X. C. Domenge and M. Ilie, "Numerical study of helicopter blade–vortex mechanism of interaction using the potential flow theory," Applied Mathematical Modelling, 36(7), pp. 2841-2857, 2012.
- [11] M. H. Mohamed, "Aero-acoustics noise evaluation of H-rotor Darrieus wind turbines," Energy, 65, pp. 596-604, 2014.
- [12] M. H. Mohamed, "Reduction of the generated aero-acoustics noise of a vertical axis wind turbine using CFD (Computational Fluid Dynamics) techniques," Energy, 96, pp. 531-544, 2016.
- [13] A. Giauque, B. Ortun, B. Rodriguez, and B. Caruelle, "Numerical error analysis with application to transonic propeller aeroacoustics," Computers & Fluids, 69, pp. 20-34, 2012.
- [14] T. F. Brooks, D. S. Pope, and M. A. Marcolini, "Airfoil self-noise and prediction," Technical Report: NASA-RP-1218, L-16528, NAS 1.61:1218, Jul 1, 1989.
- [15] N. Gregory and C. L. O'reilly, Low-Speed aerodynamic characteristics of NACA0012 aerofoil section, including the effects of upper-surface roughness simulating hoar frost, Reports and Memoranda No. 3726, Jan, 1973.
- [16] S. H. Wasala, R. C. Storey, S. E. Norris, and J. E. Cater, "Aeroacoustic noise prediction for wind turbines using Large Eddy Simulation," Journal of Wind Engineering and Industrial Aerodynamics, 145, pp.17-29, 2015.